syntheses. However, the present results show that by using the steric requirements of the bis(cyclopentadienyl) unit, the necessary structural rigidity is present to make nanometer-sized ring assemblies. It remains to be established why **3**, **4**, and **5** crystallize as closed oligomeric structures instead of open polymeric versions, but it is clear that this route to molecular supramolecular assemblies dense in uranium and nitrogen is viable.

References and Notes

1. L. Black *et al.*, *J. Alloys Compounds* **315**, 36 (2001).
2. F. G. Reshetnikov, *Atom. Energ.* **91**, 998 (2001).
3. G. P. Kushto, P. F. Souter, L. Andrews, M. Newrock, *J. Chem. Phys.* **14**, 5894 (1997).
4. N. Kaltsoyannis, *Inorg. Chem.* **39**, 6009 (2000).
5. L. Gagliardi, P. Pyykkö, *Angew. Chem. Int. Ed. Engl.* **43**, 1573 (2004).
6. C. P. Kempter, J. C. McGuire, M. R. Nadler, *Anal. Chem.* **31**, 156 (1959).
7. T. N. Le, N. Lorenzelli, L. Zuppiroli, *J. Nucl. Mater.* **184**, 230 (1991).
8. T. Urabe, K. Takahashi, M. Katsura, M. Miyake, *J. Alloys Compounds* **193**, 122 (1993).
9. I. Korobkov, S. Gambarotta, G. P. A. Yap, *Angew. Chem. Int. Ed. Engl.* **41**, 3433 (2002).
10. W. J. Evans, G. W. Nyce, M. A. Johnston, J. W. Ziller, *J. Am. Chem. Soc.* **122**, 12019 (2000).
11. W. J. Evans, G. W. Nyce, J. W. Ziller, *Angew. Chem. Int. Ed. Engl.* **39**, 240 (2000).
12. W. J. Evans, S. A. Kozimor, J. W. Ziller, N. Kaltsoyannis, *J. Am. Chem. Soc.* **126**, 14533 (2004).
13. W. J. Evans, S. A. Kozimor, J. W. Ziller, *Chem. Commum.*, in press.
14. W. J. Evans, G. W. Nyce, K. J. Forrestal, J. W. Ziller, *Organometallics* **21**, 1050 (2002).
15. W. J. Evans, S. A. Kozimor, W. R. Hillman, J. W. Ziller, *Organometallics*, in press.
16. J.-C. Bünzli, C. Piguet, *Chem. Rev.* **102**, 1897 (2002).
17. S. Krivovichev *et al.*, *J. Am. Chem. Soc.* **127**, 1072 (2005).
18. P. B. Duval *et al.*, *Angew. Chem. Int. Ed. Engl.* **40**, 3357 (2001).
19. R. Thuéry, C. Villiers, J. Jaud, M. Ephritikhine, B. Masci, *J. Am. Chem. Soc.* **126**, 6838 (2004).
20. W. J. Evans, B. L. Davis, *Chem. Rev.* **102**, 2119 (2002).
21. W. J. Evans, J. M. Perotti, J. W. Ziller, *J. Am. Chem. Soc.* **127**, 1068 (2005).
22. W. J. Evans, J. M. Perotti, J. W. Ziller, *J. Am. Chem. Soc.* **127**, 3894 (2005).
23. Materials and Methods are available as supporting material on *Science* Online.
24. D. S. J. Arney, C. J. Burns, *J. Am. Chem. Soc.* **117**, 9448 (1995).
25. R. A. Wheeler, R. Hoffman, J. Strähle, *J. Am. Chem. Soc.* **108**, 5381 (1986).
26. R. A. Wheeler *et al.*, *J. Am. Chem. Soc.* **108**, 2222 (1986).
27. J. G. Brennan, R. A. Andersen, A. Zalkin, *Inorg. Chem.* **25**, 1761 (1986).
28. W. J. Evans, S. A. Kozimor, J. W. Ziller, *Polyhedron* **23**, 2689 (2004).
29. H. Schumann, C. Janiak, J. Pickardt, *J. Organomet. Chem.* **349**, 117 (1988).
30. U. P. Singh, S. Tyagi, C. L. Sharma, H. Görner, T. Weyhermüller, *J. Chem. Soc. Dalton Trans.* 4464 (2002).
31. J.-C. Berthet, M. Lance, M. Nierlich, J. Vigner, M. Ephritikhine, *J. Organomet. Chem.* **420**, C9 (1991).
32. I. Castro-Rodriguez, H. Nakai, L. N. Zakharov, A. L. Rheingold, K. Meyer, *Science* **305**, 1757 (2004).
33. I. Castro-Rodriguez, K. Olsen, P. Gantzel, K. Meyer, *J. Am. Chem. Soc.* **125**, 4565 (2003).
34. W. P. Griffith, *Coord. Chem. Rev.* **8**, 369 (1972).
35. K. Dehnicke, J. Strähle, *Angew. Chem. Int. Ed. Engl.* **31**, 955 (1992).
36. J. G. Brennan, R. A. Andersen, A. Zalkin, *J. Am. Chem. Soc.* **110**, 4554 (1988).
37. Y. Obora, T. Ohta, C. L. Stern, T. J. Marks, *J. Am. Chem. Soc.* **119**, 3745 (1997).

38. For support of this research, we thank the Chemical Sciences, Geosciences and Biosciences Division of the Office of Basic Energy Sciences of the U.S. Department of Energy. Experimental details, x-ray diffraction data, atomic coordinates, thermal parameters, and complete bond distances and angles for **3**, **4**, and **5** are provided as supporting material on *Science* Online. Crystallographic data were deposited in the Cambridge Crystallographic Database Centre (**3**: CCDC-275800, **4**: CCDC- 275801, **5**: CCDC- 275802).

Supporting Online Material

www.sciencemag.org/cgi/content/full/309/5742/1835/DC1
Materials and Methods
Figs. S1 to S3
Tables S1 to S3
References and Notes

22 June 2005; accepted 16 August 2005
10.1126/science.1116452

Ultrahigh Strength in Nanocrystalline Materials Under Shock Loading

Eduardo M. Bringa,[1]* Alfredo Caro,[1] Yinmin Wang,[1] Maximo Victoria,[1] James M. McNaney,[1] Bruce A. Remington,[1] Raymond F. Smith,[1] Ben R. Torralva,[1] Helena Van Swygenhoven[2]

Molecular dynamics simulations of nanocrystalline copper under shock loading show an unexpected ultrahigh strength behind the shock front, with values up to twice those at low pressure. Partial and perfect dislocations, twinning, and debris from dislocation interactions are found behind the shock front. Results are interpreted in terms of the pressure dependence of both deformation mechanisms active at these grain sizes, namely dislocation-based plasticity and grain boundary sliding. These simulations, together with new shock experiments on nanocrystalline nickel, raise the possibility of achieving ultrahard materials during and after shock loading.

Dislocations are the carriers of plastic deformation in crystalline materials (*1*). The search for materials with ultrahigh hardness and strength is closely related to the search for the most effective obstacles to dislocation motion. Grain boundaries (GBs) are effective obstacles for dislocation motions (*1–3*); the strength or hardness of crystalline materials increases inversely with the square root of their grain size, a relation known as the Hall-Petch effect (*2*, *3*). As the dimensions of the grains approach nanometer sizes, this strengthening mechanism is limited by the onset of GB accommodation mechanisms, such as sliding (*2–4*). If these softening effects could be suppressed, harder materials could be created, with potential applications to such extreme environments as target capsules for the National Ignition Facility (*5*). From atomistic simulations, we show a substantial increase in strength during shock loading of nanocrystalline copper, with a complex dependence on shock pressure.

Experimental observations of increased strength have been reported in high–strain rate deformation of nanocrystalline nickel and copper, up to strain rates of 10^4 s^{-1} (*6–8*). Dislocation plasticity in nanocrystalline materials is controlled by thermal and mechanical activation of sources at GBs, a mechanism that requires fluctuations, implying an intrinsic time scale that could explain the reported strain rate sensitivity. This suggests that an increase of the strain rate by several orders of magnitude, as in shock loading conditions (*9*, *10*), may result in an even harder material. However, extrapolation of strength from a strain rate of 10^4 s^{-1} to greater than 10^6 s^{-1} becomes problematic, because strain rate cannot be increased by

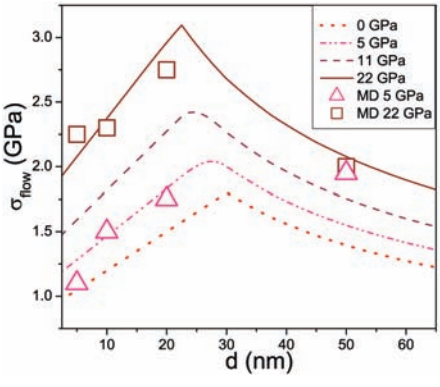

Fig. 1. Flow stress for different pressures, as a function of grain size, according to our qualitative model (*16*). MD results are also included. In this plot we use parameters from the literature or from our MD simulations (*16*): σ_0 = 0.9 GPa, α = 0.04, β = 1.0; G_0 = 45 GPa. We choose $d_0 = d_1$ = 30 nm and $\sigma_{Disl}(d_0) = \sigma_{GBS}(d_0)$ at P = 0 GPa, to obtain the only free parameter, C = 0.04.

[1]Lawrence Livermore National Laboratory, Livermore, CA 94550, USA. [2]Paul Scherrer Institute, CH-5232 Villigen-PSI, Switzerland.

*To whom correspondence should be addressed. E-mail: ebringa@llnl.gov

Downloaded from http://science.sciencemag.org/ on September 15, 2016

orders of magnitude without increasing the pressure. When uniaxial loading is due to a shock wave (i.e., a compression wave traveling faster than the sound speed), lateral relaxation does not have time to occur and pressure builds up. Under those conditions, a regime is entered where plasticity is controlled by both high strain rate and high pressure. We present atomistic simulations of shocked nanocrystalline samples, in which the extremely short compression time scales (or equivalently, very high volumetric strain rates) associated with shock loading are close to those observed in recent experiments (*10*–*12*). Such short time scales imply that dislocation creation and motion, and stress-driven GB accommodation, are the dominant plasticity mechanisms; thermally activated processes, such as diffusion, are observed to be negligible.

Both GB accommodation and dislocation activity have a pressure dependence, although for different reasons. GB accommodation has similarities to the plasticity of granular media, i.e., sliding of undeformable objects controlled by friction (*13*). In granular materials, the Mohr-Coulomb law of sliding friction predicts that the onset of plasticity occurs when the applied stress is larger than the value defined by the flow stress, $\sigma_{flow} \propto (\sigma_{coh} + \alpha\sigma_{normal})$, where σ_{coh} is related to the cohesion of the interface, and α is related to the geometry of the grains. This criterion has been recently extended to nanocrystals (*14*, *15*). Associating σ_{normal} with pressure, we conclude that the stress threshold for sliding plasticity increases linearly with pressure (*15*). Using molecular dynamics (MD) simulations, we verified that a nanocrystalline metal deforming plastically by GB accommodation gets harder as hydrostatic pressure (P) is increased (*16*) (fig. S1). With the scaling arguments presented by Van Swygenhoven and Caro (*17*) to express the dependence of deformation rate on grain size, d, the flow stress for GB sliding can tentatively be written as $\sigma_{GBS} = (\sigma_0 + \alpha P)(1 + d/d_0)$, where σ_0 is the flow stress of a zero grain size material (an amorphous metal) at zero pressure, and d_0 is a constant. Notably, σ_{GBS} increases as d increases in this regime. For shock-induced dislocation plasticity it is generally assumed that, as in the Steinberg-Guinan model (*10*), the dynamic strength and hardness of the material scales with the shear modulus, G, which in turn increases linearly with pressure, $G(P) = G_0 + \beta P$ (*10*, *16*). Adding the Hall-Petch relation, the flow stress for dislocation plasticity becomes $\sigma_{Disl} = CG(P)(d/d_1)^{-0.5}$, where β, C, and d_1 are constants. The effective flow stress for a nanocrystal can be taken as the minimum of σ_{Disl} and σ_{GBS}, although a more realistic model would include a mixture of both when $\sigma_{Disl} \sim \sigma_{GBS}$. At any pressure, as grain size decreases, the material hardens according to the Hall-Petch effect, down to the point where $\sigma_{Disl} = \sigma_{GBS}$. For smaller grain sizes, the material softens according to the law of GB sliding. As pressure increases, both mechanisms predict an increase in hardness, creating the possibility for pressure-induced ultrahard nanocrystalline materials. Figure 1 shows the qualitative hardness map that emerges from this model. These ultrahigh hardness conditions can be achieved by shock loading (*10*–*12*).

In shock loading, one surface of the system, the piston, is driven inward along the z axis at a constant velocity U_p, leading to a shock wave with velocity U_s. The first major difference between homogeneous deformation (*4*, *17*–*21*) and shock loading (*9*) is that the total volumetric strain behind the shock front, ε, is constant and determined by $\varepsilon = U_p/U_s$ ($d\varepsilon/dt = 0$) (*19*). The stress along the shock direction behind the shock front, i.e., the shock "pressure," is also constant behind the shock front and given by $\sigma_{zz} = \rho_0 U_p U_s$, where ρ_0 is the density of the preshocked material. With U_p in the range 0.1 to 3.0 km s^{-1}, the shock pressure for copper is in the range ~5 to 230 GPa. We identified hardness and flow stress with the von Mises stress, σ_{VM}, well behind the shock front, where $\sigma_{VM}^2 = 0.5[(\sigma_{xx} - \sigma_{yy})^2 + (\sigma_{yy} - \sigma_{zz})^2 + (\sigma_{zz} - \sigma_{xx})^2]$. Figure 2A shows a typical shock profile. By increasing pressure, σ_{VM} increases until the onset of plasticity occurs (peak in Fig. 2A); then it decreases and evolves in a complex way depending on factors such as strain rate, pressure, microstructure, and dislocation properties in the materials. A satisfactory quantitative theory does not yet exist. The strain rate with which the material is deformed at the shock front is roughly given by ε divided by the shock front rise time, $d\varepsilon/dt \approx \varepsilon U_s/\Delta_z$, where Δ_z is the shock front width. This width depends on a number of factors, including grain size. Portions of the sample reached by the shock wave undergo a fast deformation, $d\varepsilon/dt \sim 10^9$ to 10^{11} s^{-1}, during the short shock rise time (several picoseconds) and then remain at constant strain, eventually relaxing the shear stress. Shock loading can irreversibly freeze-in some of the microstructural changes induced during the loading, producing a residual material still harder at zero pressure after the shock. Indeed, research

Downloaded from http://science.sciencemag.org/ on September 15, 2016

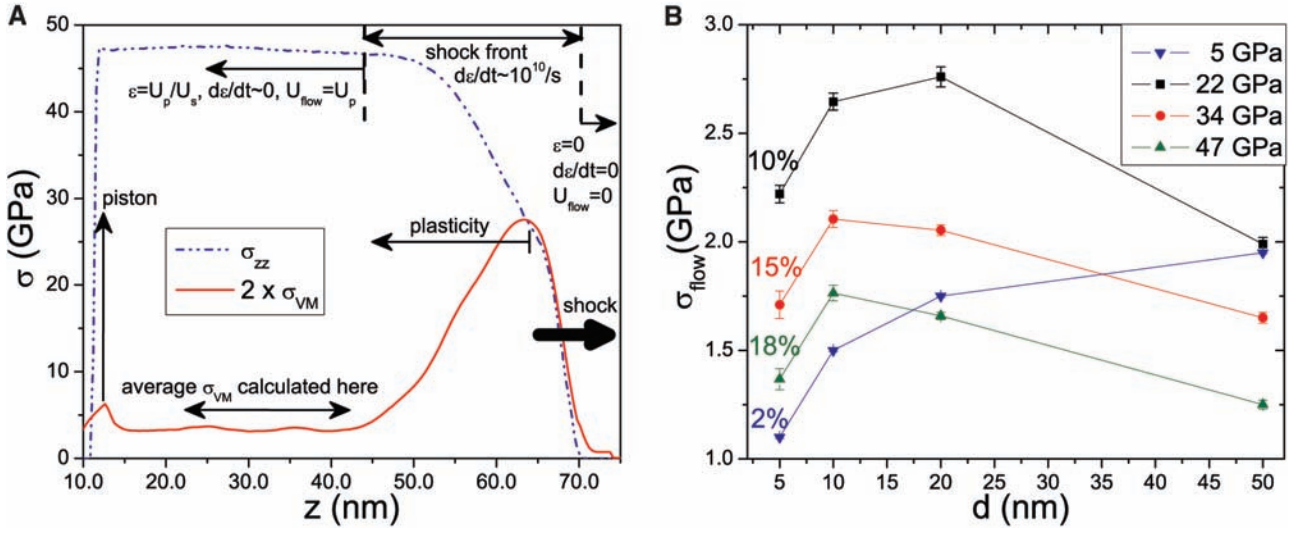

Fig. 2. (**A**) Typical stress profiles under uniaxial shock loading: σ_{zz} (shock pressure) and twice the von Mises stress. Values obtained from an image from our MD simulation ($d \sim 20$ nm), ~10 ps after the piston started to move with velocity U_p, advancing from left to right. The material has a flow velocity, $U_{flow} = U_p = 1$ km/s, giving $U_s = 5.5$ km/s, and $\varepsilon = 18\%$ behind the shock front. The shock front spreads more than in single-crystal simulations (*9*), with a width close to the grain size. (**B**) Flow stress under shock loading at different shock wave pressures (σ_{zz}). The flow stress is largest in the pressure range of 20 to 30 GPa. Total volumetric strains behind the shock front are also indicated. The flow stress was calculated as σ_{VM} averaged over ~20 nm, in a region in front of the piston, when the shock front had already traveled ~100 nm, as shown in (A). Error bars show means ± SE.

over the last several decades shows clear indications of massive modification of the material after unloading and recovering of shocked materials (*10*–*12*, *22*).

We report large-scale MD shock simulations in copper nanocrystalline samples with up to ~4 × 10^8 atoms (*16*). Shock loading conditions are ideally modeled by large-scale MD simulations (*9*, *23*–*26*), which cover time and length scales similar to laser-shock experiments. Our simulations show that the large increase in pressure substantially reduces GB sliding, limiting the softening mechanism and doubling the flow stress. As a measure of σ_{normal}, we used the shockwave pressure, σ_{zz}. The main result of this work, the flow stress as a function of grain size and pressure, is shown in Fig. 2B (fig. S2). At low stress (5 GPa), comparable to the stress of quasi-static experiments, the hardness is relatively low; there is only GB sliding (*4*, *18*), and samples with small grains are softer than those with large grains. At intermediate stress (5 to 25 GPa), the hardness at all grain sizes increases with increasing shock strength. This is the manifestation of the reduction of GB sliding and harder dislocation plasticity. MD results in this pressure range are also shown in Fig. 1, in qualitative agreement with our model. Figure 2B confirms the predicted trends, including the shift in the position of the maximum hardness toward lower grain sizes as pressure increases. At large stress (>25 GPa), a new phenomenon appears, reflected in the drop in strength (σ_{flow}) shown in Fig. 2B (fig. S2): Increased nucleation and motion of dislocations, together with a large increase in temperature, allow the sample to deform more easily. At even higher pressures (150 to 220 GPa, depending on grain size) shock-induced melting occurs, with $\sigma_{flow} \sim 0$. A maximum in hardness, therefore, exists at some intermediate pressure. We found the maximum hardness, about twice the value at "low" pressure, at ~25 GPa.

To provide insight into the atomistic processes involved in the deformation, Fig. 3 shows a 47-GPa shock wave traveling through 20-nm grains, for which only defective atoms are shown (movie S1). We observed the traces of numerous stacking faults indicating the passage of partial dislocations. Our simulations also show nanotwins, represented by mirror planes. This is similar to atomistic simulations of homogeneous deformation (*4*, *16*–*21*) and shocks (*9*, *4*–*26*) at similar grain sizes. However, the most salient feature of this figure is the presence of perfect dislocations represented by narrow ribbons of stacking faults bounded by partial dislocations inside the grains (fig. S3). The shock-induced nanotwin volume is less than 1% of the total volume at the end of our simulation. Twin growth is expected for longer pressure pulses, but experimental detection of this amount of twinning is difficult, given that a low density of twins already exists in the preshocked samples. We also found a number of defect clusters, about 1 nm in diameter, likely created by dislocation-dislocation interactions. These might act as dislocation obstacles when further deformation is carried out, contributing to increased hardness.

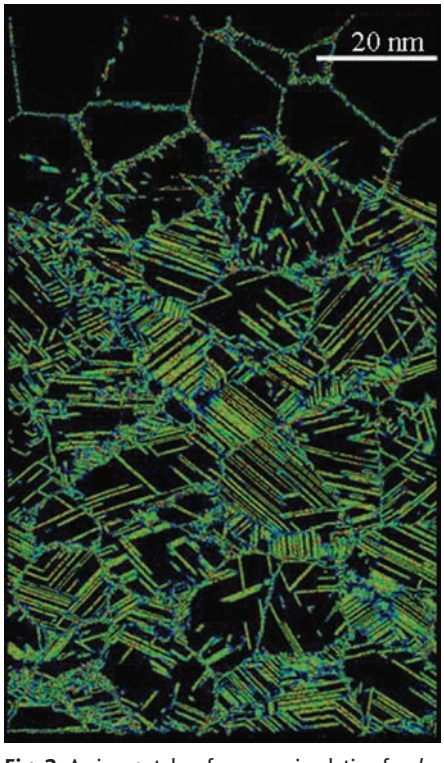

Fig. 3. An image taken from our simulation for d = 20 nm and σ_{zz} = 47 GPa. Only a thin slab (0.7 nm wide) is shown. The shock has traveled for 30 ps, from bottom to top, producing a high density of partial dislocations (attached to GBs) together with perfect dislocations ("isolated" inside grains, fig. S3) and nanotwins.

Shock-induced dislocation nucleation has been observed in numerous studies, but a detailed understanding has begun to emerge only recently. The barriers for dislocation nucleation do not increase strongly with pressure (*27*) above an initial threshold, at least in the shock regimes studied here for copper. Studies of shock waves in single-crystal copper with and without defects (*9*, *24*–*26*) show increased dislocation production with shock pressure; that is, pressure does not inhibit the nucleation process. We found the same behavior for nanocrystalline copper at all grain sizes, with a threshold of ~6 GPa, even for 5-nm grains (fig. S4). As pressure increases, dislocations nucleate initially at GB junctions (movie S2), and then from different locations along the GB. The stress is high enough to induce dislocation creation at such a small grain size, which is due to the reduction of GB sliding, a mechanism that, if dominant, would release the shear stress. This behavior can further be understood in terms of the differences in the pressure dependence of both GB sliding and dislocation-based plasticity. As the pressure increases, the grain size at which the maximum hardness occurs decreases (Figs. 1 and 2B).

In addition to the simulations shown above, we have performed experiments to understand the behavior of nanocrystalline metals under extreme conditions. Because of experimental constraints, it is very difficult to directly measure the dynamic deformation process during high–strain rate loading at the nanoscale. Figure 4 shows a plan-view transmission electron microscopy (TEM) picture of nanocrystalline nickel after shock loading at 40 GPa (*16*). Nickel and copper are both fcc materials with very similar shock impedances, but nickel has larger stacking-fault energy. There is clear evidence of dislocation activity occurring inside

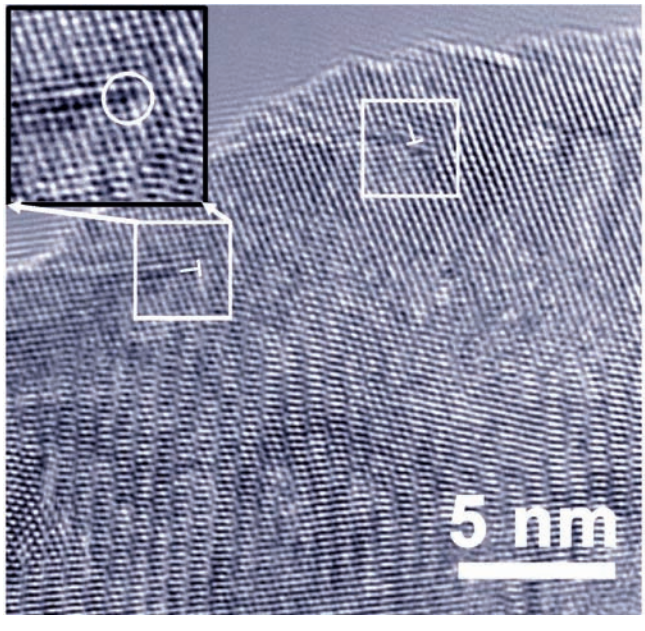

Fig. 4. A plan-view TEM image of nanocrystalline nickel after shock loading at 40 GPa. Dislocation activity is visible inside grains (white boxes); the inset shows a filtered image of the dislocation. The grain sizes before the shock loading are 30 to 50 nm. The final grain sizes are in the range 5 to 100 nm as a result of the residual shock heating in the recovered sample.

Downloaded from http://science.sciencemag.org/ on September 15, 2016

grains (boxes in Fig. 4) in agreement with our atomistic simulations. During loading at ~40 GPa, our MD simulations predict a dislocation density of $\sim 10^{13}$ cm^{-2}, which is expected to decrease during recovery. Although the exact dislocation density in recovered samples is difficult to estimate, our high-resolution TEM images do show residual dislocations inside some nanograins (Fig. 4). This is quite unusual in nanocrystalline materials and not easily achievable under normal deformation conditions (*28*). Our experiments also indicate an increase in hardness in the samples recovered after shock loading, as expected from the measured residual dislocation densities.

Computer simulations of shocks in nanocrystalline copper show that the flow stress reaches ultrahigh values at high pressures produced by shock loading. This hardness increase of up to a factor of two compared with unshocked samples arises because the barriers for GB sliding increase with pressure (*13*–*15*), whereas dislocation nucleation is not as sensitive to pressure above a threshold of several gigapascals. Although the simulations we have carried out are for nanocrystalline copper, GB sliding reduction under pressure should be a general feature of shock-loaded materials, including alloy and nonmetallic nanocrystals. Harder nanocrystalline materials could offer novel applications, including improved armor materials and National Ignition Facility targets (*5*).

References and Notes

1. R. Madec, B. Devincre, L. Kubin, T. Hoc, D. Rodney, *Science* **301**, 1879 (2003).
2. M. A. Meyers, K. K. Chawla, *Mechanical Behavior of Materials* (Prentice-Hall, Upper Saddle River, NJ, 1999).
3. J. R. Weertman, in *Nanostructured Materials: Processing, Properties and Potential Applications*, C. C. Koch, Ed. (William Andrew, Norwich, NY, 2002), pp. 397–421.
4. J. Schiøtz, K. W. Jacobsen, *Science* **301**, 1357 (2003).
5. T. R. Dittrich *et al.*, *Laser Part. Beams* **17**, 217 (1999).
6. D. Jia, K. T. Ramesh, E. Ma, L. Lu, K. Lu, *Scripta Mater.* **45**, 613 (2001).
7. L. Lu, S. X. Li, K. Lu, *Scripta Mater.* **45**, 1163 (2001).
8. F. Dalla Torre *et al.*, *Acta Mater.* **50**, 3957 (2002).
9. B. L. Holian, P. S. Lomdahl, *Science* **280**, 2085 (1998).
10. B. A. Remington *et al.*, *Metall. Mater. Trans. A* **35**, 2587 (2004).
11. M. A. Meyers *et al.*, *Acta Mater.* **51**, 1211 (2003).
12. J. M. McNaney, J. Edwards, R. Becker, T. Lorenz, B. A. Remington, *Metall. Trans. A* **35**, 2625 (2004).
13. C. A. Schuh, A. C. Lund, *Nat. Mater.* **2**, 449 (2003).
14. A. C. Lund, C. A. Schuh, *Acta Mater.* **53**, 3193 (2005).
15. B. Jiang, G. J. Weng, *J. Mech. Phys. Solids* **52**, 1125 (2004).
16. Materials and methods are available as supporting material on *Science* Online.
17. H. Van Swygenhoven, A. Caro, *Phys. Rev. B* **58**, 11246 (1998).
18. H. Van Swygenhoven, M. Spaczer, A. Caro, D. Farkas, *Phys. Rev. B* **60**, 22 (1999).
19. J. Schiøtz, F. D. Di Tolla, K. W. Jacobsen, *Nature* **391**, 561 (1998).
20. V. Yamakov *et al.*, *Nat. Mater.* **1**, 45 (2002).
21. H. Van Swygenhoven, P. M. Derlet, A. G. Frøseth, *Nat. Mater.* **3**, 399 (2004).
22. M. W. Chen, J. W. McCauley, K. J. Hemker, *Science* **299**, 1563 (2003).
23. K. Kadau, T. C. Germann, P. S. Lomdahl, B. L. Holian, *Science* **296**, 1681 (2002).
24. E. Bringa *et al.*, *J. App. Phys.* **96**, 3793 (2004).
25. F. A. Sapozhnikov, V. V. Dremov, M. S. Smirnova, *J. Phys. IV France* **110**, 323 (2003).
26. L. Davila *et al.*, *Appl. Phys. Lett.* **86**, 161902 (2005).
27. S. Cheng, J. A. Spencer, W. W. Milligan, *Act. Mater.* **51**, 4505 (2003).
28. Z. Budrovic, H. Van Swygenhoven, P. M. Derlet, S. Van Petegem, B. Schmitt, *Science* **304**, 273 (2004).

29. We thank A. M. Hodge and C. A. Schuh for help with the experiments; P. Erhart for calculating elastic constants; D. Farkas, T. Diaz de la Rubia, R. Lebensohn, M. A. Meyers, V. Bulatov, N. Park, and V. Dremov for useful discussions; M. Duchaineau for plotting the results; and Livermore Computing for MCR and Thunder time. This work was performed under the auspices of the U.S. Department of Energy at Lawrence Livermore National Laboratory under contract no. W-7405-Eng-48, with support from the Laboratory Directed Research and Development program.

Supporting Online Material

www.sciencemag.org/cgi/content/full/309/5742/1838/DC1
Materials and Methods
Figs. S1 to S4
Movies S1 and S2
References

29 June 2005; accepted 18 August 2005
10.1126/science.1116723

Influence of the Atlantic Subpolar Gyre on the Thermohaline Circulation

Hjálmar Hátún,[1,2]* Anne Britt Sandø,[3,4] Helge Drange,[3,4,5,6] Bogi Hansen,[1] Heðinn Valdimarsson[7]

During the past decade, record-high salinities have been observed in the Atlantic Inflow to the Nordic Seas and the Arctic Ocean, which feeds the North Atlantic thermohaline circulation (THC). This may counteract the observed long-term increase in freshwater supply to the area and tend to stabilize the North Atlantic THC. Here we show that the salinity of the Atlantic Inflow is tightly linked to the dynamics of the North Atlantic subpolar gyre circulation. Therefore, when assessing the future of the North Atlantic THC, it is essential that the dynamics of the subpolar gyre and its influence on the salinity are taken into account.

Formation of the densest, deepest waters of the North Atlantic THC occurs following the northward flow of warm, saline waters (the Atlantic Inflow) (Fig. 1) across the Greenland-Scotland Ridge. Through air-sea exchange, these waters subsequently lose much of their heat, but not their salt. Added freshwater from precipitation and river runoff reduces the salinity somewhat but still allows them to become the densest waters in the region. This makes the Arctic Mediterranean—the Arctic Ocean and the Nordic Seas—the dominant source area for the North Atlantic THC (*1*, *2*). Because the density close to the freezing point is mainly determined by the salinity, changes in the upper-layer salinities of this region may have large impacts on the future development of this circulation.

Climate models featuring increasing greenhouse-gas scenarios predict an intensified freshwater supply to the Arctic Mediterranean during the 21st century (*3*). Observations indicate that this is already occurring (*4*, *5*) and that large areas are freshening (*5*–*7*). This freshwater increase may partly explain why many climate models indicate a weakening of the North Atlantic THC starting from the end

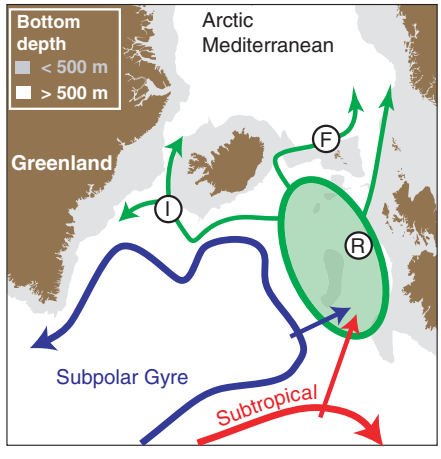

Fig. 1. Schematic of the main features of the surface circulation in the northeastern North Atlantic. The green shaded region shows where the subpolar and the subtropical waters meet, mix, and feed into the Arctic Mediterranean. The hydrographic observations used in the study are obtained in the Rockall Trough (R), Faroe Current (F), and Irminger Current (I).

[1]Faroese Fisheries Laboratory, Box 3051, FO-110, Tórshavn, Faroe Islands. [2]University of Washington, Box 357940, Seattle, WA 98195, USA. [3]Nansen Environmental and Remote Sensing Center, Thormøhlensgt. 47, N-5006 Bergen, Norway. [4]Bjerknes Center for Climate Research, Allégaten 55, 5007 Bergen, Norway. [5]Geophysical Institute University of Bergen, Allégaten 70, 5007 Bergen, Norway. [6]Nansen-Zhu International Research Centre, Institute of Atmospheric Physics, Chinese Academy of Sciences, Beijing 100029, China. [7]Marine Research Institute, Skúlagata 4, 121 Reykjavík, Iceland.

*To whom correspondence should be addressed. E-mail: hjalmarh@ocean.washington.edu

Downloaded from http://science.sciencemag.org/ on September 15, 2016

Ultrahigh Strength in Nanocrystalline Materials Under Shock Loading
Eduardo M. Bringa, Alfredo Caro, Yinmin Wang, Maximo Victoria, James M. McNaney, Bruce A. Remington, Raymond F. Smith, Ben R. Torralva and Helena Van Swygenhoven (September 15, 2005)
Science **309** (5742), 1838-1841. [doi: 10.1126/science.1116723]

Editor's Summary

This copy is for your personal, non-commercial use only.

Article Tools Visit the online version of this article to access the personalization and article tools:
http://science.sciencemag.org/content/309/5742/1838

Permissions Obtain information about reproducing this article:
http://www.sciencemag.org/about/permissions.dtl

Science (print ISSN 0036-8075; online ISSN 1095-9203) is published weekly, except the last week in December, by the American Association for the Advancement of Science, 1200 New York Avenue NW, Washington, DC 20005. Copyright 2016 by the American Association for the Advancement of Science; all rights reserved. The title *Science* is a registered trademark of AAAS.

Downloaded from http://science.sciencemag.org/ on September 15, 2016